

REPORT DOCUMENTATION PAGEForm Approved
OMB No. 0704-0188

Public reporting burden for this collection of information is estimated to average 1 hour per response, including the time for reviewing instructions, searching data sources, gathering and maintaining the data needed, and completing and reviewing the collection of information. Send comments regarding this burden estimate or any other aspect of this collection of information, including suggestions for reducing this burden to Washington Headquarters Service, Directorate for Information Operations and Reports, 1215 Jefferson Davis Highway, Suite 1204, Arlington, VA 22202-4302, and to the Office of Management and Budget, Paperwork Reduction Project (0704-0188) Washington, DC 20503.

PLEASE DO NOT RETURN YOUR FORM TO THE ABOVE ADDRESS.

1. REPORT DATE (DD-MM-YYYY) 01-15-2002		2. REPORT DATE Final report		3. DATES COVERED (From - To) 03-1998 to 6-2001	
4. TITLE AND SUBTITLE An Elasto-Dynamic Ornithoptic Flying Robotic Insect				5a. CONTRACT NUMBER	
				5b. GRANT NUMBER DABT63-98-10003	
				5c. PROGRAM ELEMENT NUMBER	
6. AUTHOR(S) Dr. Michael Goldfarb				5d. PROJECT NUMBER	
				5e. TASK NUMBER	
				5f. WORK UNIT NUMBER	
7. PERFORMING ORGANIZATION NAME(S) AND ADDRESS(ES) Vanderbilt University 512 Kirkland Hall Nashville TN 37240				8. PERFORMING ORGANIZATION REPORT NUMBER	
9. SPONSORING/MONITORING AGENCY NAME(S) AND ADDRESS(ES) Defense Advanced Research Project Agency 3701 N. Fairfax Drive Arlington VA 22203-1714				10. SPONSOR/MONITOR'S ACRONYM(S) DARPA	
				11. SPONSORING/MONITORING AGENCY REPORT NUMBER	
12. DISTRIBUTION AVAILABILITY STATEMENT Available for public distribution					
13. SUPPLEMENTARY NOTES					
20020124 409					
14. ABSTRACT The work presented in this report was focused on assessing the feasibility of piezoelectrically actuated hovering mesoscale ornithoptic flight. Four issues were investigated and addressed. The first was design and development of piezoelectrically actuated mechanisms that would generate appropriate flapping motion from piezoelectric actuation. The second was the development and characterization of aeroelastic wings that generate sufficient lift, and perhaps more importantly, optimal efficiency. The third issue was the development of and use of piezoelectric actuation that can provide (at minimum) the power-to-weight ratio required by the aeroelastic wings. Finally, the fourth issue was the development and characterization of both non-regenerative and regenerative compact power electronics for battery-powered operation.					
15. SUBJECT TERMS flapping, hovering, ornithopter, piezoelectric, resonance, regenerative, power electronics					
16. SECURITY CLASSIFICATION OF:			17. LIMITATION OF ABSTRACT	18. NUMBER OF PAGES 22	19a. NAME OF RESPONSIBLE PERSON Dr. Michael Goldfarb
a. REPORT N/A	b. ABSTRACT N/A	c. THIS PAGE N/A			19b. TELEPHONE NUMBER (Include area code) (615) 343-6924

FINAL REPORT

Title of the Effort: An Elasto-Dynamic Ornithoptic Flying Robotic Insect
Contract Number: DABT63-98-10003
Contractor: Vanderbilt University
Total Contract Period: March 1998 through June 2001
PI: Michael Goldfarb
PI Telephone: (615) 343-6924
PI Fax: (615) 343-6925
PI Address: VU Station B351592
2301 Vanderbilt Place
Nashville TN 37235

SUMMARY

The work presented in this report was focused on assessing the feasibility of piezoelectrically actuated hovering mesoscale ornithoptic flight. Four issues were investigated and addressed. The first was design and development of piezoelectrically actuated skeletal mechanisms that would generate appropriate flapping motion from piezoelectric actuation. The second was the development and characterization of aeroelastic wings that generate sufficient lift, and perhaps more importantly, optimal efficiency as measured by a lift to power ratio. The third issue was the development of and use of piezoelectric actuation that can provide (at minimum) the power-to-weight ratio (i.e., mass-specific power density) required by the aeroelastic wings. Finally, the fourth issue was the development and characterization of both non-regenerative and regenerative compact power electronics for battery-powered operation.

The significant conclusion of this work is that piezoelectrically actuated hovering ornithoptic flight at the mesoscale is not possible due to the insufficiency of actuator power density. This conclusion is based upon a combination of experiment and analysis, and is detailed in this report.

ORGANIZATION OF REPORT

Summary	
Elastodynamic Skeleton Design	2
Aeroelastic Wing Development	5
Power Density Optimization	13
Power Electronics	18
Conclusions	22

PIEZOELECTRICALLY-ACTUATED SKELETON DEVELOPMENT

The design of an elasto-dynamic ornithoptic insect is based upon several premises. The first is that moving wings are better than fixed wings at a small scale. This is due to the fact that flight (and particularly efficient flight) depends upon fluid inertial effects, and thus depends upon reasonably high Reynolds number flows. Since Reynolds numbers decrease linearly with size, smaller fixed-wing vehicles have to increase their speed linearly to maintain a given flow regime. Maintaining such speeds at small scales requires unrealistic power sources and creates significant flight control difficulties. High Reynolds numbers can alternately be achieved by moving the wings relative to the vehicle, either with an oscillatory motion (i.e., an ornithopter) or with a rotary motion (i.e., a helicopter). The former enables the use of an electromechanical resonance, which significantly increases actuation efficiency, and further creates a vehicle with significantly greater stealth characteristics than a helicopter approach, since in nature there exists a large number of similar-sized ornithopters.

Multiple PZT-actuated insect skeletons were designed and fabricated. The two approaches that were successful were based respectively on four-bar and five-bar kinematic mechanisms. The skeleton shown in Figure 1, prototype DM1, utilizes a carbon fiber spar as the primary aerostructure, weighs approximately 5.5 grams, and flaps the wings shown approximately 20 degrees at 15 Hz. The skeleton in Figure 2, prototype DM2, which is a variation on the design of Figure 1, also weighs approximately 5.5 grams and generates a significantly greater amplitude of motion than the design of Figure 1, but at a slightly lower frequency. Specifically, the design of Figure 2 generates approximately 50 degrees of motion at about 13 Hz. The skeleton of Figure 3, prototype ACG2, which incorporates a five-bar mechanism, weighs approximately 6.0 grams and flaps the wings shown approximately 25 degrees at 13 Hz. The prototype DM6, shown in Figure 5, generates a wing root motion of 50 degrees at a structural resonant frequency of 18 Hz (with the wings shown). The mechanism is actuated by a pair of four-bar linkages that operate near a kinematic singularity. The total weight of the prototype is 22.1 grams. This prototype is somewhat heavier and larger than previous prototypes, since it was designed to be a higher-powered device. Prototype GF4, shown in Figure 5, generates approximately 60 degrees of wing motion at a frequency of approximately 40 Hertz. Finally, in order to increase the effective wing area and to minimize inertial imbalances due to flapping, we developed four-winged designs, such as prototype MG2 shown in Figure 6. This prototype can generate wing root amplitudes of 40 degrees at a resonant frequency of 11 Hz with the wings shown. The prototype weighs approximately 29 grams. The general conclusion from constructing these several prototypes is that piezoelectric actuation can produce appropriate motion for small-scale ornithoptic flight.

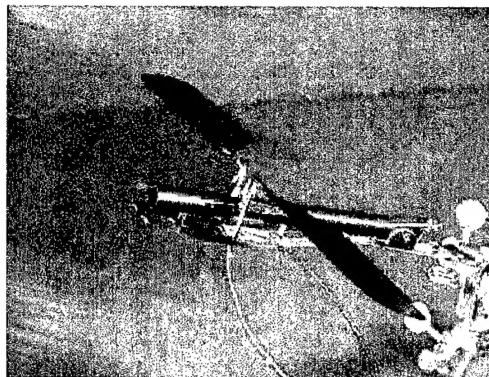


Figure 1. Prototype DM1.

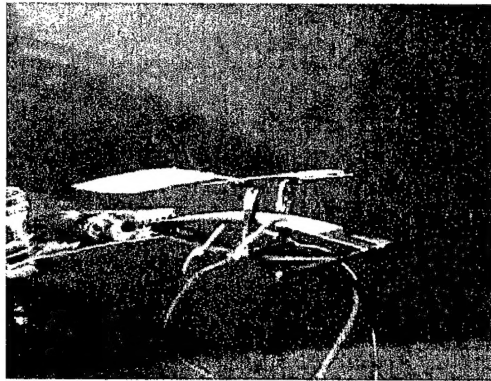


Figure 2. Prototype DM2.

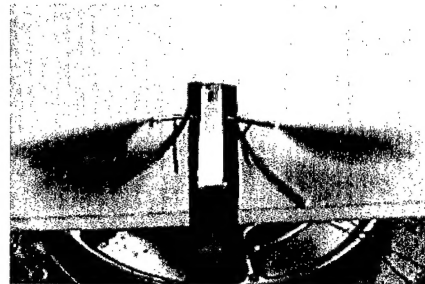
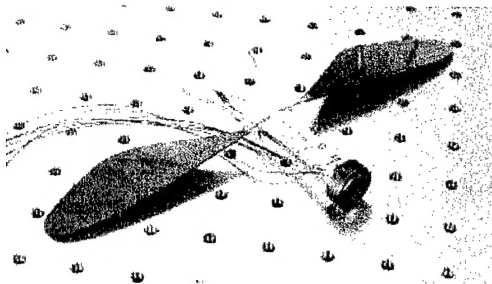


Figure 3. Prototype ACG2.

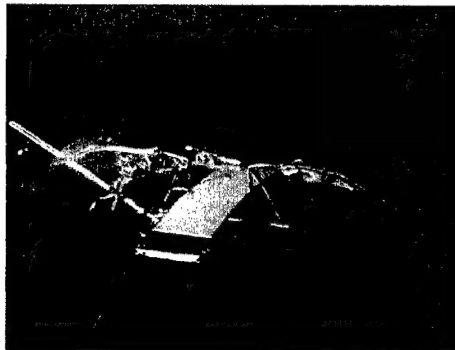


Figure 4. Prototype DM6.

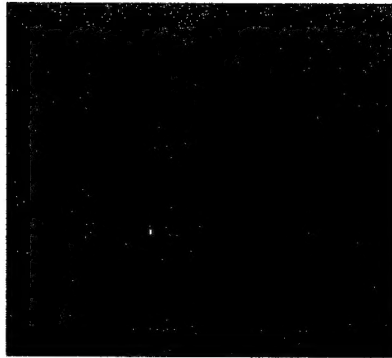


Figure 5. Prototype GF4, which generates wing amplitudes of sixty degrees at approximately 40 Hertz (without wings).

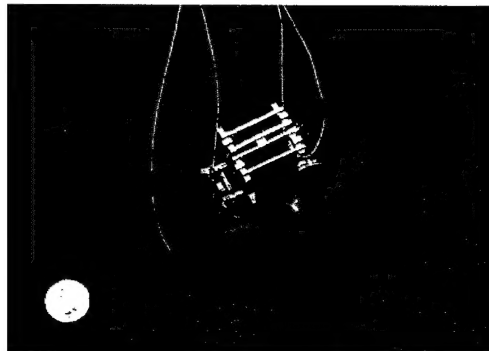


Figure 6. X-wing prototype that generates wing amplitudes of forty degrees at approximately 11 Hertz, for a total wing sweep of 160 degrees.

AEROELASTIC WING DEVELOPMENT AND TESTING

The objective of the wing development work was to quantify some of the fundamental parameter influences on the performance of flapping wings in order to develop wings with an optimal lift to power ratio, referred to as the wing efficiency. The efficiency with which flapping wings generate thrust forces is strongly dependent on the phase lag between translational and rotational wing articulation. The primary objective is therefore to investigate a method of wing construction that results in an optimal relationship between flapping wing bending and twisting such that optimal thrust forces are generated. The desirable aeroelastic coupling between wing bending and twisting is established through wing construction techniques and materials. Experiments aimed at measuring the wing thrust and power were carried out in order to quantify the wing performance. Figures 7 and 8 show the experimental flapping rig developed for wing characterization, and some of the several wings developed for characterization, respectively.

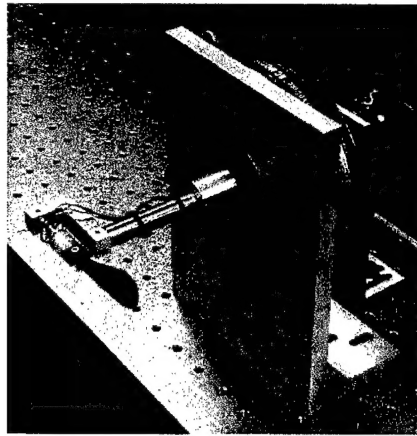


Figure 7. Computer-controlled wing testing machine.

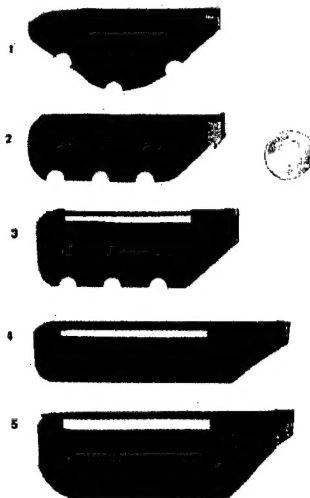


Figure 8. Various carbon fiber wing designs.

Experimental Set-Up

A test bed, as shown in Figure 9, was built in order to measure the instantaneous thrust forces and power usage of different wing designs. This rig consisted of a low inertia DC motor to create flapping motions with of pre-selected frequency and amplitude. Wings were connected to the motor shaft by a full bridge strain gauge load cell which measured the instantaneous thrust produced by the wing during flapping. A second load cell was employed to measure the power required to sustain flapping motions. Data was acquired with a *dSpace* digital signal processing system which collected motor shaft position and velocity information as well as load cell data. The DSP system was also used to trigger a high speed video camera. The video was then synchronized with the position and thrust data.

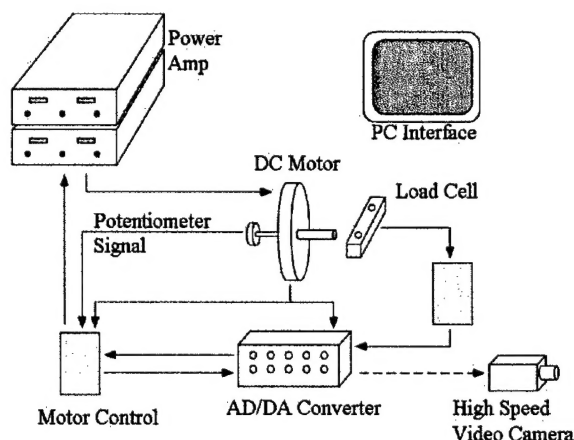


Figure 9. Schematic of the experimental rig.

Lift data was collected using a binocular load cell design as shown in Figure 10. A full bridge strain gage circuit was used, consisting of four semiconductor gages bonded to the aluminum device. The load cell was oriented to measure horizontal forces, ignoring any net vertical forces. Power measurements were made using a simpler beam-type load cell design. The beam-type load cell also used a full bridge strain gage configuration, but employed foil-type gages. The binocular load cell was used for thrust measurements since its design is insensitive to the location of the applied force. Conversely, the beam type load cell, with gages on either side of the beam, measured moment. The distance of the applied force from the load cell is directly proportional to the output signal. As a result, the binocular load cell was calibrated for force, while the beam-type load cell was calibrated for moment. These calibration factors were applied during post-processing to convert the gage voltage signals to forces and moments. Following calculation of the forces or moments using the calibration factors, the data was filtered through a zero phase digital Butterworth filter in *MATLAB*.

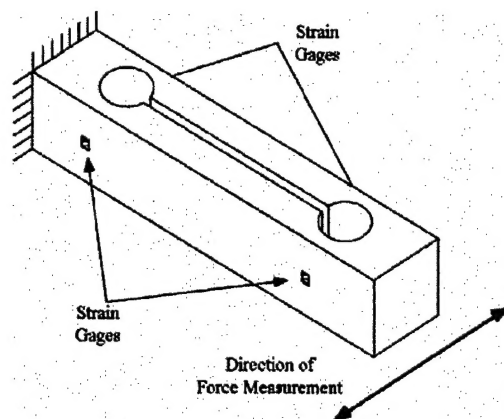


Figure 10. Depiction of the load cell.

To correlate the aeroelastic wing behavior during flapping to the beneficial and detrimental wing thrust peaks, captured wing thrust data was synchronized with high-speed video recordings of the wing in motion. Thrust data acquisition and the high-speed video camera were captured simultaneously using *dSpace* to obtain matching data and video. To correlate the point in time shown by the wing video with the appropriate data point, a moving timeline was superimposed on the thrust data.

Synchronization was accomplished through the implementation of a *dSpace* function which triggered the high-speed camera to begin recording at a known point in the thrust data collection process. Video of the flapping wing was recorded at 500 frames per second and matched with data for three full stroke cycles. Using *Adobe Premiere* video editing software, the high-speed video of the wing was synchronized with an animation of the thrust data plot, including the timeline to denote the location of the data corresponding to the wing video. The two videos were superimposed upon one another to create a single video file.

All wings were constructed with a similar planform in order to preserve the geometric similarity. The wings were made with milar sheet which is stiffened by carbon-fiber “ribs”. One rib comprised the leading edge of the wings while 4 other ribs ran in the chord direction. The primary change in wing construction was the width and thickness of the leading edge stiffener. By varying this member the bending natural frequency could be tuned over a wide range. The wings had a roughly rectangular shape with a span of 6 inches and an aspect ratio of 2.3.

The primary objective in wing construction was to develop wings that possess specific relationships between their translational and rotational motion. This desire was based on the findings which indicated that the phase lag between wing translation and rotation is critical to the efficient production of thrust. However, the articulation of these wings is constrained to a single degree of freedom, i.e. wing root rotation. Therefore, the specified articulation would have to be achieved through passive elastic design. This was achieved by tailoring the natural frequencies of the fundamental wing bending and torsion modes. Assume that the fundamental wing bending and torsion modes are independent, second order oscillators with equal natural frequencies. When these two oscillators are excited by the same input they will respond with equal phase relative to the input. In other words, the wing bending (translation) and wing torsion (rotation) will be in phase. Now suppose that the bending natural frequency is twice the torsional natural frequency. If the wing is excited by an input at the torsional natural frequency then the torsional response will lag the input by 90 degrees. However the excitation frequency is half of the bending natural frequency so that the bending response is nearly in phase with the excitation. The net result is that the torsional (rotation) will lag the bending (translation) by 90 degrees. Therefore, by

simply tuning the natural frequencies of the wing we are able to achieve a range of lag and lead phase between translation and rotation.

Results

The primary objective of these experiments was to quantify the importance of various, fundamental non-dimensional parameters on the production of thrust by flapping wings. The parameters under investigation are listed in Table 1 along with the parameters that were varied to study the effects.

Non-Dimensional Parameter	Definition	Associated Dimensional Parameter
Coefficient of Thrust, C_T	$C_T = \frac{F}{\frac{1}{2} \rho v^2 l^2}$	Measured parameter
Reynolds Number, Re	$Re = \frac{\rho v l}{\mu}$	Flapping Amplitude
Wing Frequency Ratio, γ	$\gamma = \frac{\omega_b}{\omega_f}$	Wing bending and torsional stiffness
Excitation Frequency Ratio, η	$\eta = \frac{\omega_e}{\omega_f}$	Excitation Frequency

One of the primary objectives was to develop a desirable bending/torsion motion in the wing with a single degree of freedom excitation. This was motivated by the findings of Dickinson et al (1999). In this work, it was established that the relative phase between wing translation and rotation is crucial to the optimal development of thrust. However, typical biological aviators have several degrees of freedom with which they articulate their wings. Our goal was to achieve a similar wing articulation with only a single degree of freedom. This was to be accomplished by tuning the wing bending and torsion natural frequencies of the wing as described previously.

As outlined previously, several wings were tested with wing frequency ratios ranging from 0.5 to 2.5. Results for two of these wings will be presented in detail. The first is the wing whose bending and torsional natural frequencies were 20 Hz resulting in a wing frequency ratio of $\gamma=1.0$. The wing was excited with a 20 degree amplitude. A snapshot of the synchronized video is shown in Figure 4. The oscillating trace shows the instantaneous thrust, the vertical line indicates the time of the frame and the horizontal line indicates the average thrust produced. Note that the wing is moving down and has just passed the point of producing maximum thrust. The wing articulates such that the bending (or translation) motion is in phase with the torsional (or rotational) motion.

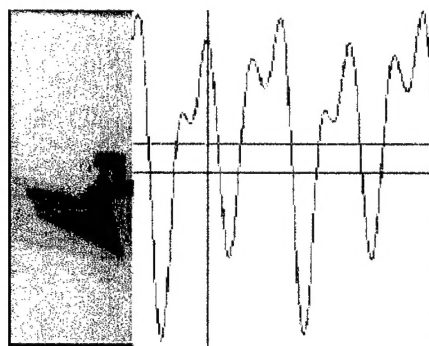


Figure 11. Synchronized video/data frame for the $\gamma=1$ wing.

One interesting aspect of the instantaneous thrust data shown in Figure 11 is the small “dip” in the thrust as the wing approaches the point of maximum thrust. This was at first attributed to nonlinear bending dynamics in the wing. However, recent results from CFD modeling of 2-D rigid flapping wings have noted a similar effect. In the computational work the “dip” was attributed to the vortex separation from the wing. Future synchronization of flow visualization with thrust data will seek to verify this effect. A second aspect of the thrust data to note is how the thrust data, which occurs at a frequency twice the flapping frequency, exhibits an asymmetry in the negative thrust portion of the data. This is due to a slight asymmetry in the wing construction. The carbon-fiber stiffening ribs were glued to only one side of the wing. Therefore, the wing has a small stiffness asymmetry that results in different behavior on the up and down strokes.

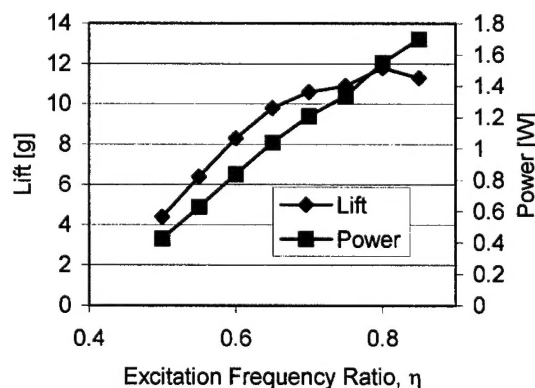


Figure 12. Thrust and power data for the $\gamma=1$ wing.

Lift and power data are summarized in Figure 12 for the $\gamma=1.0$ wing. This figure shows the average thrust generation and required power over a range of frequencies. Note that the thrust peaks at a value of 12 grams and at an excitation frequency that is approximately 80% of the bending and torsion natural frequencies. As expected, the power required to sustain the flapping motion increases linearly with frequency.

The second wing for which detailed data are provided had a bending natural frequency of 40 Hz and a torsional natural frequency of 22 Hz resulting in a wing frequency ratio of $\gamma=2.0$. A frame of the synchronized video is shown in Figure 13. In this case the wing articulates such that the torsional motion lags the bending motion by 90 degrees. This is the type of wing articulation employed by *drosophyllia* as

noted by Dickinson et al.(1999) The fact that the wing is being excited at torsional resonance and well below the bending resonance is apparent in Figure 6 as indicated by the large chord-wise deformation of the wing and small span-wise deformation.

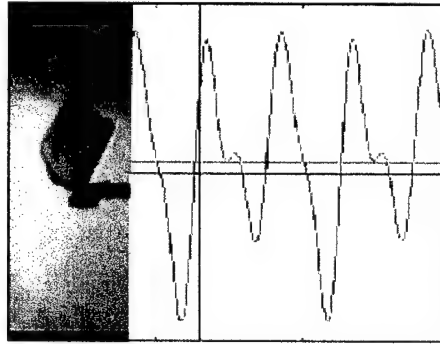


Figure 13. Synchronized video/data frame for the $\gamma=2$ wing.

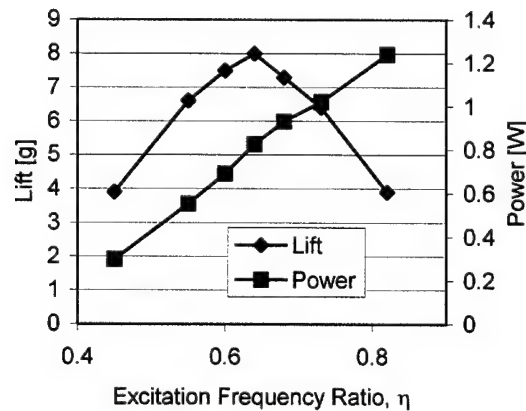


Figure 14. Thrust and power data for the $\gamma=2$ wing.

The lift and power data for this wing are shown in Figure 14. Again, the plot shows the instantaneous thrust, the average thrust and the time of the wing video frame relative to the thrust data. As in the previous case the maximum thrust is generated somewhat below the torsional natural frequency. Of particular interest is the fact that the maximum thrust generated by this wing is less than that generated by the wing with a wing frequency ratio of 1. This was somewhat unexpected since it has been noted that *drosophylla* wing articulation is of this nature.

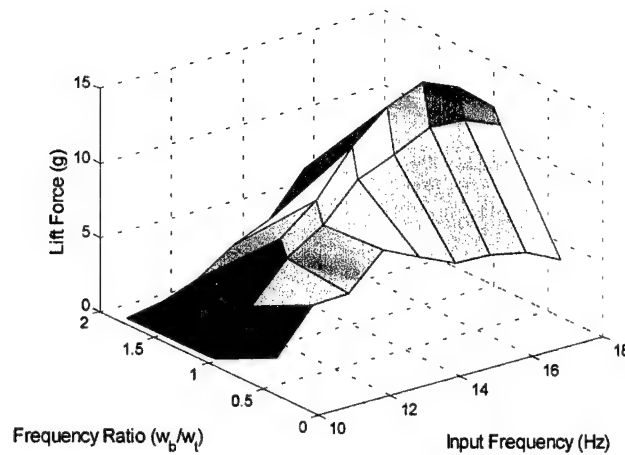


Figure 15. Thrust force for a variety of wings and excitation frequencies.

This trend held over a range of wing frequency ratios as summarized in Figure 15, which shows the thrust, generated by several wings possessing different wing frequency ratios. Overall, the wing that produced the maximum thrust was the one with a wing frequency ratio of 1. Two interesting phenomena are illustrated in this plot. One is that the maximum thrust is generated by the wing frequency ratio 1 wing for all excitation frequencies. The second is that the maximum thrust is generated at an excitation frequency that is below the torsional resonant frequency.

One plausible explanation for why the *drosophyllia* type wing articulation does not generate the maximum thrust is shown in Figure 16. This figure shows the thrust to power ratio for both the wing frequency ratio 1 and 2 wings. This metric is proportional to the efficiency of the wing. Note that although the wing frequency ratio 1 wing produces the most thrust, the wing frequency ratio 2 wing (which is similar in articulation to that of *drosophyllia*) exhibits the maximum efficiency. So it appears that in this case nature has chosen optimum efficiency over optimum performance.

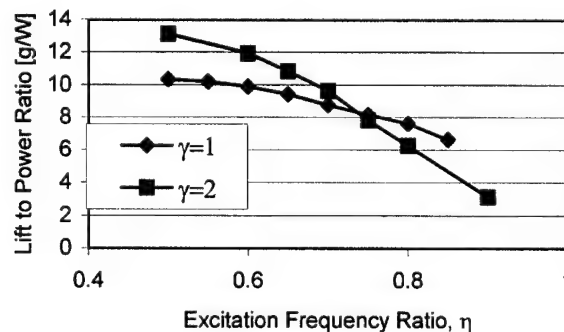


Figure 16. Wing flapping thrust to power ratio.

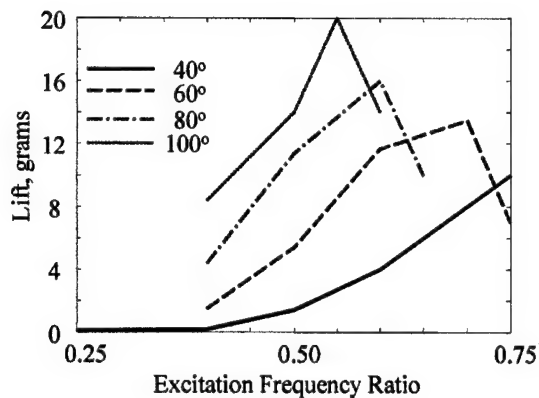


Figure 17. Thrust generated at various flapping amplitudes.

The final result addresses the fact that the maximum thrust generated by all wings occurs at a frequency somewhat below the torsional natural frequency. It was expected that the most thrust would be generated at resonance since this would result in the maximum displacement. However, as shown in Figure 17, the frequency of maximum thrust drops with flapping increasing amplitude. In fact, the maximum thrust generation is produced at the frequency, which results in the maximum torsional displacement. However, as the flapping amplitude increases the aerodynamic loading results in an effective added mass to the wing, which lowers the resonant frequency.

Perhaps the most significant result from our extensive wing testing is that, as long as the first bending mode is equal to or greater than the first torsional mode, wings exhibit very similar lift characteristics. Further, all wings seem to achieve a peak power-to-lift ratio of approximately 8 grams per Watt in the region in which they generate maximum lift. This would indicate that in order to achieve hovering flight, a power supply and actuation system must be capable of generating at least 125 mW/g. The following section investigates this issue.

POWER DENSITY OPTIMIZATION

Maximum Power Density of PZT Actuator

Analysis determined that the maximum power density delivered from a commercial unimorph actuator (Thunder model 8R) is 382 mW/g. Specifically, phasor modeling techniques were employed to determine the maximum power output available from a commercial PZT unimorph actuator for a given load. The combined actuator and aeroelastic load is modeled as a force input with a second order actuator impedance in series with a second order load impedance. The model of the actuator was experimentally validated. For the modeled system, the output power can be written in terms of model impedances as:

$$P_{out} = \frac{1}{2} V_m^2 \text{Re}(Z_l)$$

where

$$Z_a = b_a + j\omega(m_a - \frac{k_a}{\omega^2})$$

$$Z_l = b_l + j\omega(m_l - \frac{k_l}{\omega^2})$$

$$Z_t = Z_a + Z_l$$

$$V = V_m \cos(\omega t + \phi) = \frac{F_m}{Z_t} = \frac{F_m \left[(b_a + b_l) - j\omega(m_a + m_l - \frac{k_a + k_l}{\omega^2}) \right]}{(b_a + b_l)^2 + \omega^2(m_a + m_l - \frac{k_a + k_l}{\omega^2})^2}$$

Using these equations, an expression for output power can be written as:

$$P_{out} = \frac{F_m^2 b_l}{2(b_a + b_l)^2 + 2\omega^2(m_a + m_l - \frac{k_a + k_l}{\omega^2})^2}$$

It can be shown that the output power of the system is maximized with respect to frequency when operated at the system resonance, in which case the expression reduces to:

$$P_{out} = \frac{F_m^2 b_l}{2(b_a + b_l)^2}$$

With respect to the damping coefficients, P_{out} is maximum when $b_l = b_a$ or

$$2\gamma_a \sqrt{k_a m_a} = 2\gamma_l \sqrt{k_l m_l}$$

These equations were used to analyze the maximum possible power output of a commercially available PZT actuator, the Face TH-8R THUNDER unimorph. Table 1 shows some of the actuators properties. The mass, stiffness, and damping ratios were determined experimentally with the actuator in a cantilever beam configuration. It can be shown that the power delivery to a dynamic load is maximized when the

load impedance is described by the complex conjugate of the source (i.e., actuator) impedance. Therefore, for purposes of determining the maximum possible power output, the mass, stiffness, and damping ratio of the load were set to be equal to the TH-8R's properties. When operated at the system resonant frequency, the power output of the actuator was 0.764 W. Since the actuator has a mass of 2 grams, the power density of the TH-8R is 382 mW/g. As previously mentioned, hovering flight requires approximately 125 mW/g. A 10 gram bug would therefore require 1.25 W to hover. According to this analysis, if the maximum power transfer can be achieved, the 10 g ornithopter will only require 3 g of actuator weight. Recall, however, that the load properties were arbitrarily set to be exactly equal to that of the actuator in order to optimize power density. This would almost certainly never be the case in a practical application. Further, analysis of the model indicates that the output power decreases significantly if the load is not matched to the actuator. Additionally, the output power is inversely proportional to the system damping coefficient, even when the system is impedance matched.

F_m	0.23 N
m_a	0.77 g
k_a	169 N/m
b_a	0.00865
ω_n	468 rad/s

Table 1: Face TH-8R THUNDER actuator properties. Note that the model mass, m_a , is the appropriate dynamic mass to describe the first mode of a cantilevered beam, and not the actuator mass.

Analytical feasibility of PZT-actuated flapping flight

As described in the previous section, PZT actuators, when driving a perfectly matched impedance, possess sufficient power density to sustain hovering flight. The question remains, can PZT actuators produce sufficient energy density when driving wings? In order to address this issue, a thorough effort in the optimization of an actuator for PZT-actuated flapping flight was conducted. As shown in Figure 18, frequency response data was obtained and utilized to form a model of the impedance of a flapping wing. The wing model was interfaced with a model of a PZT actuator in order to optimize the design of the actuator for maximum power density and for maximum lift generation. A schematic representation of the combined actuator/wing model is shown in Figure 19. We initially conducted the optimization with a previously published model based on a PZT bimorph actuator (Lobontiu, N., Goldfarb, M., and Garcia, E. Achieving Maximum Tip Displacement during Resonant Excitation of Piezoelectrically-Actuated Beams. *Journal of Intelligent Material Structures and Systems*, vol. 10, no. 11, pp. 900-913, 2000). Since our device utilizes a pre-stressed unimorph, however, we reconstructed the PZT model to accurately reflect the characteristics of unimorph actuators. In comparing the two models against experimental data, the newly formulated model was shown to describe the experimental results significantly better than the former model, as demonstrated in Tables 2 through 4. Given this new model, the results for the power density and net lift generated by the optimal solutions for PZT actuators are shown in Figure 20. Clearly, the net lift is always negative, which indicates that PZT-actuated flight (at this scale and with these wings) is not possible. Using data from TRS Ceramics, we further conducted an optimization for a design utilizing PZN-PT (single crystal PZT), which is shown in Figure 21. Though performance was significantly better than the PZT version, the optimization indicates that the single crystal version is also not capable of sustaining hovering flight.

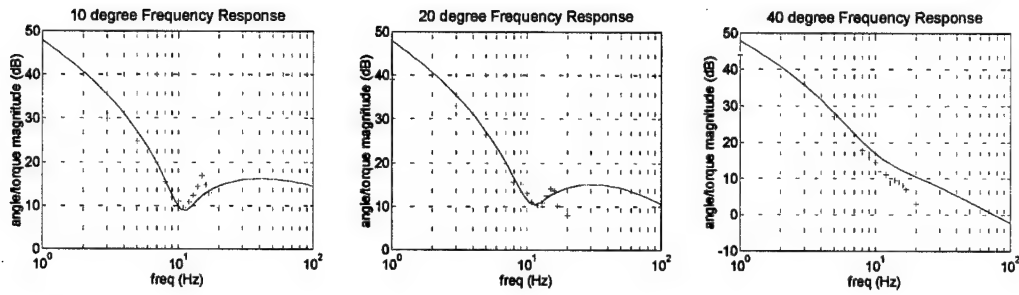


Figure 18. Frequency response data (red) and associated models (blue) for an aeroelastic wing.

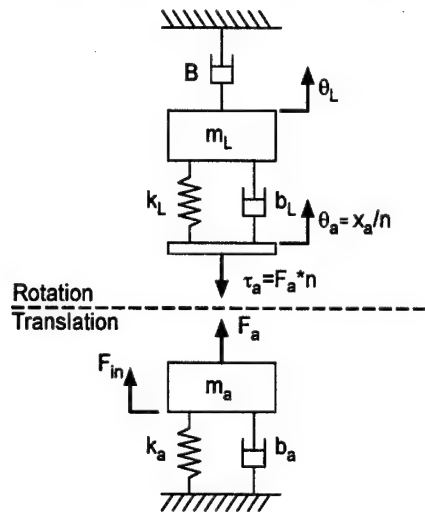


Figure 19. Schematic of dynamic model utilized for optimization.

THUNDER PZT model	Displacement from catalog [mm]	Displacement from bimorph model [mm]	Displacement from unimorph model [mm]
6-R	3.12	2.1	3.3
7-R	7.62	5.4	7.5
8-R	1.98	1.9	2.1

Table 2. Displacement comparison on 1 Hz.

THUNDER PZT model	Resonance frequency from catalog [Hz]	Resonance frequency from bimorph model [Hz]	Resonance frequency from unimorph model [Hz]
6-R	60	140	63.7
7-R	31	55	32.0
8-R	65	150	68.5

Table 3. Resonant frequency comparison.

THUNDER PZT model	Blocking force from experiment [N]	Blocking force from bimorph model [N]	Blocking force from unimorph model [N]
6-R	1.6	2.7	1.5
7-R	1.3	1.4	1.0
8-R	0.23	0.32	0.17

6-R	Mass [kg]	Stiffness [N/m]	Damping [Ns/m]	Force [N]
Old	0.0032	2612	0.09	2.7
new	0.0146	1838	0.15	1.5

7-R	Mass [kg]	Stiffness [N/m]	Damping [Ns/m]	Force [N]
Old	0.0045	541	0.046	1.4
new	0.0175	564	0.094	1.0

8-R	Mass [kg]	Stiffness [N/m]	Damping [Ns/m]	Force [N]
Old	0.00035	334	0.01	0.32
new	0.0018	408	0.025	0.16

Table 4. Blocking force comparison.

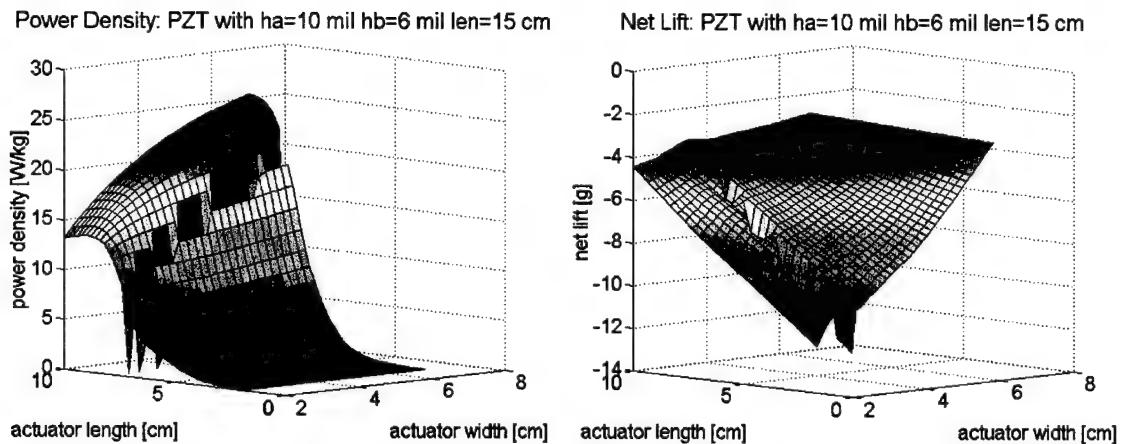
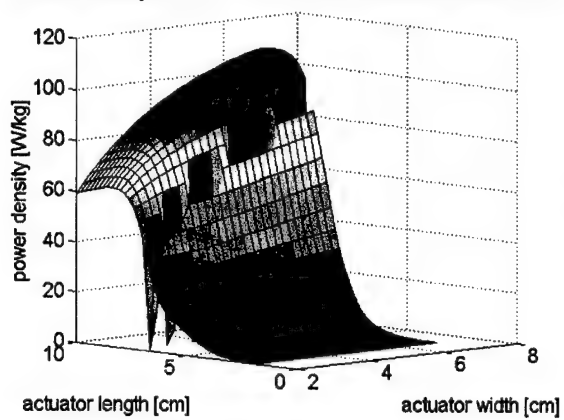


Figure 20. Power density and net lift for PZT-actuated flapping flight.

Power Density: PZN-PT with $h_a=10$ mil $h_b=6$ mil $l_{en}=15$ cr



Net Lift: PZN-PT with $h_a=10$ mil $h_b=6$ mil $l_{en}=15$ cm

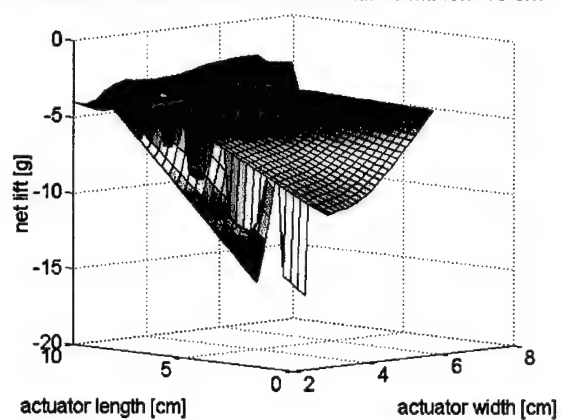


Figure 21. Power density and net lift for PZN-PT-actuated flapping flight.

POWER ELECTRONICS

Non-regenerative Square-Wave Driver

Figure 22 shows a square-wave driver that generates a ± 150 volt square wave output with adjustable frequency from 5 to 70 Hz. The driver measures approximately 4.5 cm by 4.5 cm and weighs approximately 16 g (without a battery). This type of driver is simple and efficient, since it utilizes open-loop operation and the switching occurs at the output frequency (~ 10 Hz). The primary drawback to such a design is the significant inefficiency that results from driving a resonant device (i.e., the robot) with a square wave. Since square waves contain significant energy at frequencies other than the fundamental frequency, use of a square wave greatly reduces the amount of energy directed at the fundamental frequency, and therefore greatly reduces the efficiency of energy transmission to the mechanical frequency of interest.

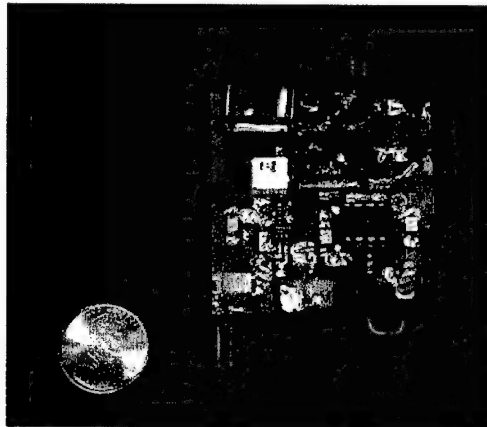


Figure 22. Second prototype of non-regenerative power electronics. The circuit outputs a ± 150 V square wave voltage with frequency adjustable from 5 to 70 Hz.

Non-regenerative Sine-Wave Driver

Figure 23 shows a dual-output sine-wave driver that generates dual 90 degrees phase-shifted ± 240 volt sinusoids wave with adjustable frequency from 1 to 30 Hz. The driver is about 5 cm x 10 cm and weighs approximately 37 g (without a battery). The circuit is powered by a Li/MnO₂ NEDA-5024LC battery (3 volts, 650 mAh, 16 grams). Since this driver generates sinusoids, essentially no mechanical energy is lost at the fundamental frequency. Since the driver requires closed-loop operation and more importantly since the PWM switching occurs at about three orders of magnitude above the output frequency (~ 10 kHz), the electrical losses are significantly higher than square wave drivers and closed-loop components add to the size and weight. Consequently, there is a trade-off between the loss of mechanical energy at the fundamental frequency in a square wave driver versus the loss of electrical energy in the switching in a sine wave driver, as well as the added size and weight of the latter.



Figure 23. Top and bottom view of third generation non-regenerative power electronics.

Regenerative Sine-Wave Driver

Regenerative electronics have the ability to recover reactive power previously delivered to the load. The regenerative electronics that were developed are based on a bi-directional flyback converter, which unlike a (more typical) unidirectional flyback converter, can move energy in both the forward and backward directions. Unidirectional and bi-directional flyback converters are shown in Figure 24 and 25, respectively. Figure 26 shows a functional diagram of the regenerative circuit, which utilizes closed-loop control of a pair of bi-directional flyback converters to generate a sinusoid of ± 240 volt amplitude. Figure 27 shows the 2nd generation prototype of the circuit.

This circuit was simulated and experimentally tested to assess the amount of energy recovered by the regenerative electronics driving a purely capacitive load. The results of these tests are shown in Figure 28. The circuit was shown to recover approximately 50% of the power delivered to the capacitive load. The recovered power, however, comes at the added cost of additional baseline dissipation introduced by the additional (MOSFET) switches of the bi-directional flyback converter. Specifically, power recovery requires the bi-directional converters, which in turn require twice the number of switches and thus twice the switching losses of an “equivalent” non-regenerative converter. The regenerative system entails further losses (relative to the non-regenerative) due to the fact that power is flowing both directions across the transformers, and the added current flow introduces additional resistive and eddy current losses within the transformers. For the circuit developed, the regenerative version entailed about one Watt of baseline dissipation in the switching, as compared to an “equivalent” non-regenerative, which (due to the issues just mentioned) would entail between $\frac{1}{4}$ and $\frac{1}{2}$ of a Watt. The baseline dissipation was measured to be essentially independent of load frequency, which is expected, since the switching frequency is constant at about 60 kHz. The amount of power recovered by the regenerative circuit is a function of the amount of RMS power delivered to the load, which increases linearly with output frequency and inversely with load capacitance. At low output frequencies, the amount of power recovered is small relative to the amount of baseline dissipation. At higher frequencies, however, the recovered power becomes significant relative to the baseline dissipation of the regenerative circuit. As seen in Figure 28, for this load and output amplitude, a non-regenerative circuit is a more efficient means of driving the stated capacitive load below frequencies of 50 Hz, while a regenerative circuit is more efficient for frequencies about 70 Hz.

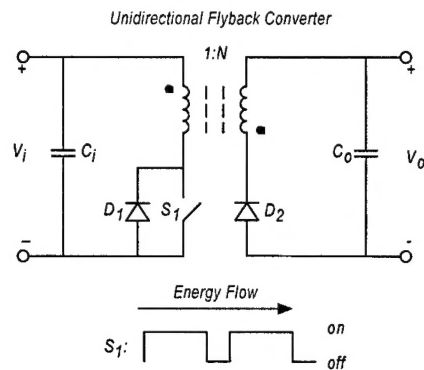


Figure 24. Unidirectional flyback converter.

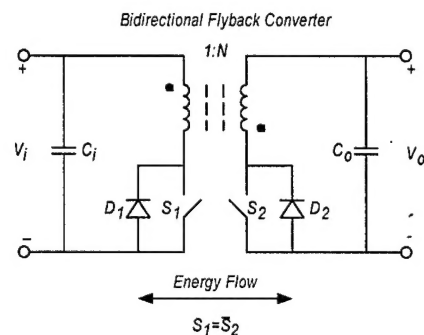


Figure 25. Bidirectional flyback converter.

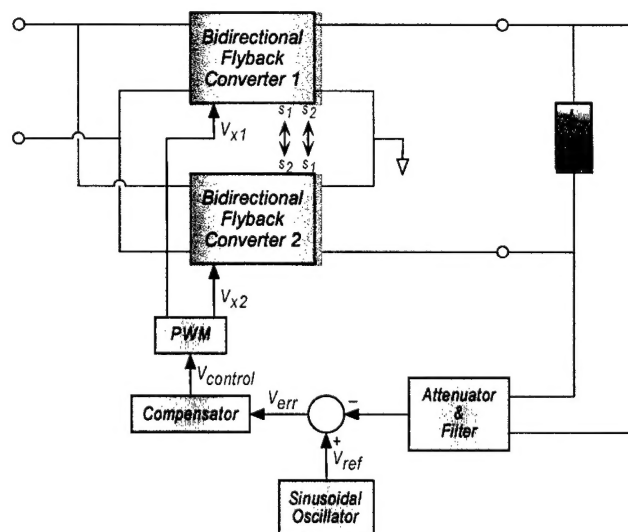


Figure 26. Functional schematic of closed-loop PWM-controlled regenerative circuit.

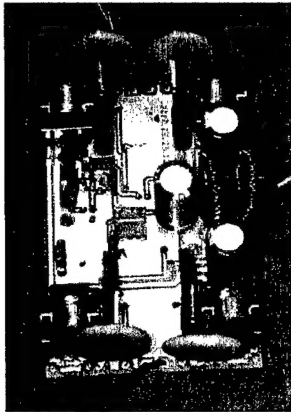


Figure 27. 2nd generation prototype of regenerative circuit.

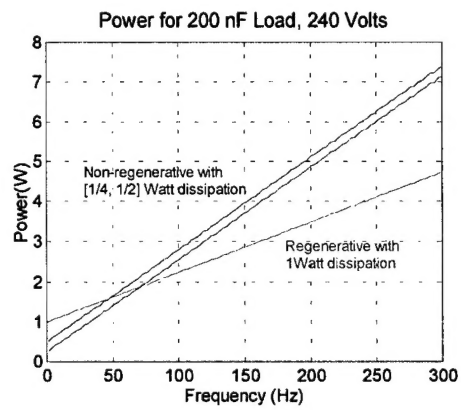


Figure 28. Comparison of regenerative versus non-regenerative power electronics for a 200 nF capacitive load with a sinusoidal amplitude of 240 volts.

CONCLUSIONS

Piezoelectric actuation has been shown to be capable of generating the *motion* required of ornithoptic flight, but was also shown to be incapable of generating the power required to sustain flapping hovering flight at the mesoscale. Specifically, it appears that mesoscale aeroelastic wings generate approximately 8 grams of lift per Watt of input power in their region of maximum lift. The power supply/actuation system must therefore supply a power density requirement of at least ~ 125 mW/g. Analysis demonstrated that PZT is capable of providing well over this power density when driving a perfectly impedance-matched harmonic load. Due to the dynamic character of aeroelastic wings, however, PZT fundamentally cannot achieve maximum power density. As a result, PZT may or may not be capable of generating the power density required for hovering ornithoptic flight. An optimization based on experimental measurements indicated that PZT-actuated mesoscale hovering ornithoptic flight is not possible.

With regard to power electronics issues, a trade-off exists between square-wave and sine-wave generators. Specifically, there is a trade-off between the enhanced mechanical efficiency of sine wave output and the reduced size, weight, and electrical power losses of square wave drivers. There is also a trade-off between regenerative versus non-regenerative power electronics, and specifically between the increased baseline dissipation of the regenerative types versus the amount of power regenerated. The latter is a function of the RMS power delivered to the load, which is a function of the output frequency and load capacitance.